

Multiple CaMKII binding modes to the actin cytoskeleton revealed by single molecule imaging\*

**S. Khan<sup>^</sup>, I. Conte, T. Carter, K. U. Bayer & J. E. Molloy**

*<sup>^</sup>Corresponding author*

*\*Running title: Single CaMKII molecule binding to F-actin*

---

## **ABSTRACT**

Localization of the  $\text{Ca}^{2+}$ /calmodulin-dependent protein kinase II (CaMKII) to dendritic spine synapses is determined in part by the actin cytoskeleton. We determined binding of GFP-tagged CaMKII to tag-RFP labelled actin cytoskeleton within live cells using total internal reflection fluorescence microscopy and single molecule tracking. Stepwise photo-bleaching showed CaMKII formed oligomeric complexes. Photo-activation experiments demonstrated that diffusion out of the evanescent field determined track lifetimes. Latrunculin treatment triggered coupled loss of actin stress fibers and the co-localized, long-lived CaMKII tracks. The CaMKII $\alpha$  ( $\alpha$ ) isoform previously thought to lack F-actin interactions also showed binding, but this was three-fold weaker than CaMKII $\beta$  ( $\beta$ ). The  $\beta\text{E}'$  splice variant bound more weakly than  $\alpha$ ; showing binding by  $\beta$  depends critically on the inter-domain linker. Mutations  $\beta\text{T287D}$  and  $\alpha\text{T286D}$  that mimic auto-phosphorylation states also abolished F-actin binding. Auto-phosphorylation triggers “autonomous” CaMKII activity but does not impair GluN2B binding, another important synaptic protein interaction of CaMKII. The CaMKII inhibitor tatCN21 or CaMKII mutations that inhibit GluN2B association by blocking binding of ATP ( $\beta\text{K43R}$ ,  $\alpha\text{K42R}$ ) or  $\text{Ca}^{2+}$ /calmodulin ( $\beta\text{A303R}$ ) had no effect on the interaction with F-actin. These results provide the first rationale for the reduced synaptic spine localization of the  $\alpha\text{T286D}$  mutant, indicating that transient F-actin binding contributes to the synaptic localization of the CaMKII $\alpha$  isoform. The track lifetime distributions had stretched exponential form consistent with a heterogeneously diffusing population. The heterogeneity suggests that CaMKII adopts different F-actin binding modes, most easily rationalized by multiple subunit contacts between the CaMKII dodecamer and the F-actin cytoskeleton that stabilize the initial, weak (micro-molar) monovalent interaction.

## INTRODUCTION

The calcium calmodulin dependent kinase (CaMKII) is a multi-functional kinase that has a prominent role in long-term potentiation (LTP) (1-3). The four major isoforms of vertebrate CaMKII have around forty splice variants and are expressed in diverse tissues (3). Two isoforms, CaMKII $\alpha$  ( $\alpha$ ) and CaMKII $\beta$  ( $\beta$ ), are dominant in the brain and their relative expression levels vary in different regions of the brain and also during development (4). Their relative levels also vary within individual neurons between the cell body, dendritic and axonal processes (2). CaMKII has a prominent structural role in hippocampal dendritic spines, the post-synaptic computational units for LTP. CaMKII concentration in spines is high (5), consistent with the structural role. The  $\beta$  isoform targets  $\alpha\beta$  heterooligomers to dendritic spines by binding to the spine actin cytoskeleton (6). Synaptic stimulation triggers CaMKII sequestration to dendritic spines and the postsynaptic density (PSD) within a few seconds of stimulation (7-10). The rapid sequestration is coupled to actin polymerization and expansion of the stimulated spine (11). Expansion is due to the direct effects of CaMKII on the actin cytoskeleton (12, 13) as well as indirect effects, mediated through activation of other kinases (14). The spine size increase persists after termination of the stimulus-induced calcium transient. CaMKII levels in stimulated spines are also increased, due to association with the PSD, in particular the NMDA receptor GluN2B subunit (15) and the enlarged actin cytoskeleton (16). In the longer term, CaMKII promotes axonal branching and outgrowth (17).

The neuronal isoforms have highly homologous kinase and association domains, but the linker that connects these two domains is variable in sequence and length (1). The individual subunits assemble into homo- or hetero-oligomers of variable isoform composition and the atomic structure of the dodecameric enzyme has been described (18). The  $\alpha$  and  $\beta$  isoforms form 12 subunit homo-oligomers of similar size, with one study reporting a slightly smaller  $\beta$  oligomer (19). Calmodulin binding to the regulatory segment relieves inhibition and trans-phosphorylation activates the enzyme at  $\alpha$ T286 (T287 in the other isoforms) which confers autonomous activity to the enzyme.

Binding of  $\beta$  but not  $\alpha$  to the actin cytoskeleton has been shown by various approaches including co-localization, fluorescence photo-bleaching and pharmacological manipulations in neuronal and non-neuronal cell culture (6, 20-23). *In vitro* sedimentation assays and electron microscopy have demonstrated  $\beta$ -dependent formation of F-actin bundles (12, 22-24). Activation of  $\beta$  by auto-phosphorylation and the phospho-mimetic, T287D, mutation (22) both abolish actin bundling activity. Furthermore, an alternative splice variant ( $\beta'$ ) that has a short linker (similar to  $\alpha$ ) does not bind or bundle F-actin in pull-down assays. Differences seen with the mutants in pull-down assays were consistent with co-localization in neuronal cell cultures. Pyrene fluorescence measurements (12) show that both  $\alpha$  and  $\beta$  isoforms bind globular (G-) actin and  $\beta$  binds with 2.4  $\mu$ M affinity and a stoichiometry of 12 actin monomers per oligomer (24). However, quantitative estimates of the affinity of either  $\beta$  or  $\alpha$  for F-actin and the modulation by activation, either through stimulation or mutation, are not available.

Here, we characterize the association of CaMKII with labelled F-actin in live human umbilical vein endothelial cells (HUVECs) (25) using total internal reflection fluorescence microscopy (TIRFM) to image and track single molecules (26, 27). We have previously exploited this approach to study motor proteins, ion channels and G-protein coupled receptors (27-30). We extend the method here to measure the association of enhanced green-fluorescent protein (GFP) tagged CaMKII native and mutant proteins with a red fluorescent protein (RFP) tagged actin to mark the cytoskeletal structures. Single molecule tracking experiments have shown that actin depolymerization increases CaMKII mobility in dendritic spines and that different, heterogeneous mobility distributions obtain for stimulated versus un-stimulated states (16). We have used HUVECs as a model system because they are ideal for TIRF imaging, have defined cytoskeletal architecture and are amenable to transient transfection methods. Our measurements show that both neuronal CaMKII isoforms bind cytoskeletal actin, but with affinities that differ by three-fold over the first decade range of a log-

### *Single CaMKII molecule binding to F-actin*

normal binding curve. Our results explain why association of  $\alpha$  might have been overlooked in earlier studies and have implications for CaMKII transport and cytoskeletal remodeling within neurons.

## MATERIALS & METHODS

All bio-chemicals were sourced from Sigma-Aldrich (Poole Dorset, UK) unless noted otherwise.

### 1. Total Internal Reflection Fluorescence Microscopy (TIRFM)

The custom-built TIRF microscope workstation was based around an inverted microscope (Nikon Eclipse, TE 2000U, Nikon, Kingston-upon-Thames, UK) (**Figure 1**). Complete details are provided in **Section SA1 in the Supporting Material**.

**Figure S1: TIRF workstation.** Choice of laser excitation wavelength (laser 1 = 561 nm; laser 2 = 488 nm) was computer-controlled; excitation (green line) and fluorescence emission (red arrow) light paths are shown. The TIRF incident angle was adjusted by an external mirror. The microscope stage and objective lens employed piezo-positioners to control specimen position and image focus. Images were acquired by an EMCCD camera. A waveform generator set the duration, delay and frequency of photo-activation pulses (laser 3 = 405 nm) also in TIRF mode. Separate, exchangeable filter-cassettes were used for GFP or tRFP fluorescence.

### 2. In vitro Assays

As a single fluorophore calibration specimen, GFP molecules were immobilized onto the surface of a microscope flow-cell using a GFP antibody by first filling the flow-cell with phosphate buffered saline (PBS) solution (pH 7.4) containing 5 µg/ml (3 nM) polyclonal anti-GFP antibody (Abcam, Cambridge, UK) as reported previously (27). This solution was left to incubate in the flow-cell for 5 min and then washed with PBS supplemented with 0.5mg/ml bovine serum albumin (BSA), to block regions of bare cover-glass. The solution was then replaced with PBS containing 10 ng/ml (0.37 nM) GFP (Clontech, Palo Alto, CA) for 5 minutes and unbound protein was washed out of the flow-cell by several washes with "Assay Buffer", AB<sup>-</sup> (20mM Imidazole, (pH 7.4), 50mM KCl, 2mM EGTA, 4mM MgCl<sub>2</sub>) before viewing by TIRFM. The molecules were imaged in degassed and argon purged AB<sup>-</sup> supplemented with an oxygen scavenger system consisting of 3 mg/ml glucose, 0.5 mg/ml catalase, 0.2 mg/ml glucose oxidase and 20mM dithiothreitol. Using the antibody-immobilized GFP molecules as a control sample the single fluorophore intensity was measured as a function of excitation power. The average value measured over several hundred fluorophores was linear with laser power. The mean single fluorophore intensity could therefore be used as an independent, internal, check of excitation power in our subsequent experiments.

### 3. Cell Culture

CaMKII fusion proteins tagged with monomeric eGFP (GFP) or photo-activatable eGFP (PaGFP) carrying the A206K mutation, have been described previously (22, 31-34). The GFP tag does not interfere with kinase activity or holoenzyme assembly (24); while immuno-electron microscopy has shown native CaMKII sequesters to the PSD of dendritic spines (35) with kinetics similar to those reported by the tagged proteins (36, 37). The following tagged actin fusion proteins were studied: mCherry-actin (38), tagRFP-actin (39) and mTurquoise2-actin (40). We chose tagRFP-actin (tRFP-actin) for its brightness, photo-stability and expression level (41). The plasmids encoding GFP-CaMKII and tRFP-actin constructs were mixed and co-transfected into primary HUVEC or Cos7 cells at 70-80% confluence primarily by nucleofection (Lonza Nucleofector Model-2b, Blackley, UK). Alternatively, Lipofectamine-2000 (Life Technologies, Paisley, UK) transfection was used as described (42). Transfection efficiency, with either method, was typically greater than 50%. The cells were plated on poly-lysine coated dishes (Lab-Tek, chambered borosilicate, #1 cover-glass, Nunc, Rochester, NY, USA) in DMEM medium with added 10% fetal bovine serum and streptomycin (50 µg/ml). Cell culture dishes were removed from the CO<sub>2</sub> incubator (*Galaxy R*, Scientific Laboratory Supplies, Ltd, East Riding, Yorks, UK,) between 24 to 36 hours after transfection. These incubation

## *Single CaMKII molecule binding to F-actin*

times were optimal for visualization of single GFP-CaMKII molecules. TIRF imaging was conducted at 25°C within an hour after removal from the incubator.

The HUVECs chosen as a model system for most of our TIRF imaging experiments attach firmly to the culture dish substrate and have long ventral stress fibers (43) that form oriented arrays. Other cytoskeletal substructures; namely arcs (44) and filopodia are also present. Although HUVECs express a variant CaMKII $\delta$ 6 isoform (45), they do not natively express the  $\alpha$  or  $\beta$  isoforms found in neurons. Expression was monitored by epi-fluorescence, and cell morphology with phase-contrast. In addition to morphology, integrity of physiological state was checked for by noting absence of CaMKII aggregation caused by high pH or calcium (36).

### *4. Single Molecule Image Analysis*

A typical experiment involved a set of co-transfections of the plasmid encoding tRFP-actin with a plasmid encoding a GFP-CaMKII fusion (two dishes per CaMKII construct; up to four constructs per experiment). Control dishes, co-transfected with plasmids encoding tRFP-actin and GFP-CaMKII $\beta$  were included in each experiment to assess primary culture viability. First, tRFP-actin fluorescence was used to identify transfected cells; then GFP-fluorescence was recorded. Many thousands of single particle tracks were obtained for each construct using >12 cells from 4 different culture dishes and 2 separate experiments. Details of the single particle tracking algorithm and the analytical measures used are in **Sections SA2, SA3 in the Supporting Material**.

Multiple analysis of variance (ANOVA) and simultaneous pairwise t-tests were conducted in R (<https://www.r-project.org/>) as detailed in (46). Variance was the sum of the variation within groups and between groups normalized by their degrees of freedom. The probability (p-value) that differences between populations are significant was then computed from the F-value (F). Significant differences reported by ANOVA were then tested by performing simultaneous, pairwise, t-tests with default Holm correction for multiple testing.

## RESULTS

Our experimental study had two parts: **(A)** Dual-color TIRFM was used to visualize and track (27) individual, GFP-tagged  $\langle\alpha\rangle$  and  $\langle\beta\rangle$  isoforms in HUVECS and properties were derived from population statistics and spatial co-localization with F-actin cytoskeletal structures. **(B)** Different mutants and pharmacological agents were then studied in order to understand the structural basis of CaMKII association with F-actin.

### A. Assay Development

#### 1. Visualization of GFP molecules in control specimens and live cells –

Antibody-immobilized GFPs were visualized at low surface density ( $<1 \mu\text{m}^{-2}$ ) using TIRFM to establish the emission intensity of individual GFP molecules under our standard imaging conditions. Individual GFPs were readily identified as discrete fluorescent spots that had a diffraction-limited point spread function (PSF) with a characteristic spot intensity (**Figure 2A**). The spots had a mean duration of  $2.0 \pm 0.4\text{s}$  and exhibited single-step photo-bleaching with a unitary intensity of  $27.4 \pm 2.2$  counts/pixel. Brighter spots with two-fold greater intensity exhibited two-step photo-bleaching (**Figure 2B**). Next, TIRFM video recordings were made of cultured HUVEC and Cos7 cells that were expressing GFP. In contrast to the video recordings of antibody-immobilized GFP molecules, the GFP fluorophores within cells could not be resolved (**Figure 2C**). This was because rapid diffusive motion within the cytosol caused image blurring during the frame acquisition period as explained below.

**Figure 2: TIRFM visualization of GFP in vitro and in living cells versus GFP-CaMKII. Ai** Antibody immobilized GFP molecules (10-frame averaged image). **ii.** Line intensity profiles of the four spots in field center, top and right ( $\pm$ standard error (se), thin line) and of the brighter spot (arrow) show diffraction-limited size. **B.** Intensity vs time records of spots shown in **Ai** illustrating single step photo-bleaching (**i, ii, iii**), blinking behavior (**iv**), and double-step photo-bleaching of the brighter spot (**v**). The single-step modal value was  $27.5 \pm 2.5$  counts/pixel (doubling and tripling occurs when fluorophore PSFs overlap). **C.** Single video frame (50ms exposure) of a HUVEC expressing GFP alone shows that motion blurring prevents single fluorophore observation. **D.** Single video frame of HUVEC expressing GFP-CaMKII $\beta$  shows that discrete fluorescent spots are now visible.

#### 2. Visualization of homomeric GFP-CaMKII $\beta$ complexes in the cellular cortex –

In marked contrast to cell cultures expressing GFP molecules alone (see above), single fluorescent particles were visualized by TIRFM in cell cortices when GFP-tagged  $\langle\beta\rangle$ , henceforth  $\beta$ , was expressed (**Figure 2D**). The basis of the discrepancy can be explained by the spot intensity being attenuated by motion-blurring during the 50ms frame acquisition period ( $\delta t$ ). The attenuation factor of the computed centroid is given by ratio of the area covered by the diffusing particle during a single video frame =  $\pi(\delta x)^2$  (where  $\delta x = (4D\delta t)^{1/2}$ , D is diffusion coefficient) and the area that captures 90% of the object's PSF (here a 3x3 pixel region on the camera) =  $0.9 \mu\text{m}^2$ .

The expected lateral diffusion coefficients,  $D_{Stokes}$ , for the relevant species were computed from the diffusion equation (Equation 1):

$$D_{Stokes} = \frac{k_b T}{6\pi\eta a_s} \quad \text{Equation 1}$$

## Single CaMKII molecule binding to F-actin

Stokes radius  $a_s = (3M/4\pi A\sigma)^{1/3}$   $M$  = molecular weight (kiloDaltons (kDa)),  $A$  = Avogadro's number,  $\sigma$  = protein density ( $1,300 \text{ kg/m}^3$ ) (47),  $\eta$  = cortical viscosity ( $0.0032 \text{ Pa}\cdot\text{s}$ ) (48, 49); giving an estimated,  $D_{Stokes}$  for GFP ( $M = 27\text{kDa}$ ;  $a_s \sim 2 \text{ nm}$ ) of  $\sim 30 \mu\text{m}^2\text{s}^{-1}$  and diffusive motion blurring during a 50ms video frame of  $\sim 20 \mu\text{m}^2$ . So, the expected reduction in fluorescence intensity (per pixel) is  $20/0.9 \sim 23$ -fold. This explains why freely diffusing GFP molecules were not resolved at video imaging rates. Since  $D_{Stokes}$  varies inversely as the cube-root of the molecular weight we were also unable to resolve the GFP- $\alpha$ , henceforth  $\alpha$ , mutant that is monomeric due to deletion of the association domain ( $\alpha\Delta 316$ ) ( $M=62\text{kDa}$ ) and tRFP-G-actin ( $M=70\text{kDa}$ ) as both exhibit more than 15-fold estimated attenuation of spot intensity due to motion blurring. The fact that we were able to satisfactorily visualize  $\beta$  is because they form dodecameric complexes ( $M = 87 \times 12 = 1044\text{kDa}$ ) (18, 50). Thus, the intensity attenuation by motion blurring ( $\sim 7$ -fold) is more than compensated for by the 12-fold increase in intensity due to the increased number of GFPs.

### 3. Decoration of actin stress fibers with single GFP-CaMKII $\beta$ holoenzymes –

We used two-color TIRFM to image  $\beta$  (excited at 488nm) and tRFP-actin (excited at 561 nm) in order to characterize  $\beta$  complexes interacting with F-actin cortical structures. TIRFM of HUVECs, transfected with t-RFP actin revealed long linear fibers in the actin cortex. The morphology was consistent with ventral stress fibers (43), and these structures will henceforth be referred to as such. About 100 video frames could be averaged, to enhance the relatively static fibers above the background of rapidly diffusing G-actin monomers. The averaged tRFP-actin image could then be overlaid onto TIRFM video recordings of  $\beta$  molecules to reveal their movement within the cytosol and their association / dissociation with the tRFP-tagged F-actin structures (**Movie S1 in the Supporting Material**).

Individual GFP-fluorescent spots were identified and tracked in the video sequences to yield spatiotemporal trajectories (300-3,000 per record) of individual objects. Tracks were generated by linking centroids for successive frames. Apparent diffusion coefficients ( $D_{lat}$ ) were computed from the centroid frame-to-frame displacements ( $\Delta x$ ).

$$D_{lat} = (\Delta x)^2 / (4t^c) \quad \text{Equation 2}$$

For free diffusion,  $c = 1$ . For confined diffusion,  $c > 1$  and denominator pre-exponent  $< 4$ . Individual tracks terminated when the object intensity dropped below the detection threshold, due either to diffusion from the excitation region (evanescent field), photo-bleaching or tracking errors (considered below). Superposition of the image showing all of the particle tracks obtained over one video-record (lasting 25 seconds) onto the averaged tRFP-actin image provided a measure of co-localization (Pearson's correlation coefficient,  $P_{pix}$ ) as described (Section SA1). It was clear that  $\beta$  associated with the cortical actin fibers (**Figure 3A**).

**Figure 3: CaMKII $\beta$  decoration of the actin cytoskeleton visualized by two-color TIRFM. A.** Averaged images of  $\beta$  (left panel, green, 400 frames) and tRFP-actin (right panel, red, 100 frames). Mean tRFP intensity =  $119 \pm 9$  counts / pixel. Lower panels (arrow) show the two frames superimposed ( $P_{pix} = 0.27$ ,  $P_{rand} = 0.09 \pm 0.07$ ) (left) and the single particle tracks (right) accumulated over 10 seconds of video (Movie S1). **B.** MSD versus time interval ( $\Delta t$ ) for the total population of tracks (white circles), short-lived (yellow circles) and long-lived (blue circles) track sub-populations ( $\pm$  standard deviation ( $\sigma$ )). The initial gradient of the short-lived track data gives  $D_{lat} = 0.28 \mu\text{m}^2/\text{s}$  while the long-lived tracks give  $0.04 \mu\text{m}^2/\text{s}$ . Total number of tracks,  $n = 12,723$ . **C.** Intensity histograms for the short-track sub-population (yellow bars) and long-track sub-population (blue bars). Asterisk (black) marks region

of histogram used to analyze photo-bleaching. **D.** Sample intensity versus time plots for some of the objects from the asterisk-marked region. Step-wise intensity changes as detected by running Student's *t* test (Fig. S1) are marked immediately below each trace to indicate sudden intensity transitions. The starting intensity for each spot was >170 counts/pixel which is ~8-fold greater than the unitary GFP intensity. The green line (in the lowest panel), is the two-step immobilized GFP photo-bleaching, redrawn from **Figure 2Bv**, shown as reference.

#### 4. Interaction dynamics between CaMKII $\beta$ and the actin cytoskeleton –

Automated single particle tracking (27) was used to identify and track individual  $\beta$  complexes. The object tracks were characterized with measures defined in Materials and Methods. Short-lived particle trajectories ( $t < 0.58$ s, **Figure 3B**, yellow symbols) closely approximated Brownian motion. In contrast, the plot for longer-lived trajectories ( $t > 2.5$ s, **Figure 3B**, blue symbols) was non-linear with little increase in the MSD beyond  $\Delta t > 1.2$  s. Further analysis showed that the binned sub-population of short-lived tracks had a unimodal intensity distribution with lower mean relative to the parent population, whereas the sub-population of longer-lived tracks had higher intensity relative to the parent population and the intensity distribution was greatly skewed towards higher values (**Figure 3C**). The different sub-population characteristics are consistent with the notion that tracks from weakly-bound, more mobile molecules have short duration and dominate the  $< 0.5$  s sub-population. In contrast, more strongly-bound molecules dominate the  $> 2.5$  s sub-population, with lower average  $D_{lat}$ . The modal intensities, for both sub-populations, are lower than expected for the multimeric (10-12 subunits) tagged  $\beta$  holoenzymes. Thus while the correlation between intensity and mobility differences might first seem simply due to a difference in aggregate size it is better explained by intensity attenuation due to motion blurring (section 2). To ascertain this was the case we examined single spots and tracks.

In order to test for multi-subunit state we measured step-wise changes in fluorescence intensity. Spots immobilized on actin stress fibers had the highest intensities but PSF-limited spatial profiles similar to single GFP fluorophores (Figure 2A). A small subset of such spots was analyzed (**Figure 3D**). The average initial intensity was ~8-fold greater ( $171.6 \pm 11.5$  counts/pixel) than measured for individual GFP molecules *in vitro* (~27 counts/pixel). We used a running Student's *t*-test to detect significant jumps in local mean intensity over adjacent sections of data (**Fig S1 in the Supporting Material**). The mean intensity drop for each stepwise change in intensity was  $22.1 \pm 2.0$  counts/pixel and the mean step duration,  $2.6 \pm 0.4$  s, similar to values for single GFP molecules immobilized *in vitro* ( $27.4 \pm 2.2$  counts/pixel and  $2.0 \pm 0.4$  s). Many of these spots showed a several fold greater final intensity drop (e.g. 90  $\rightarrow$  0 counts/pixel (spot v)) relative to the  $27.4 \pm 2.2$  counts/pixel drops obtained for single GFP photo-bleaching. Simultaneous photo-bleaching of multiple (3 for spot v) GFP fluorophores is not likely. Instead, the final intensity drops presumably report dissociation of  $\beta$  holoenzymes from the fibers and diffusion out of the evanescent field before all their fluorophores have bleached.

Sample tracks and their MSD vs.  $\Delta t$  plots were analyzed next (**Fig S2 in the Supporting Material**). In addition to high intensities, long-lived tracks had highly non-linear MSD vs.  $\Delta t$  plots with the MSD and  $\Delta t$  correlation abolished for intervals greater than a few frames, consistent with immobilization as validated by examination of the single tracks. Centroid intensity inversely correlated with mobility in the short-lived tracks of diffusing spots, with values consistent with the motion-induced 7-fold attenuation relative to the intensity of immobilized holoenzymes. The slopes (MSD vs.  $\Delta t$ ) of these short tracks correlated with the time-fraction during which they were mobile. The analyses of the single spot photo-bleaching and single tracks show that motion blurring is responsible for the observed mobility – intensity correlations between the sub-population distributions. We conclude that the rapid decrease in the track population with time is governed predominantly by diffusion of unbound molecules out of the evanescent field.

*5. Filopodia kymographs support the tracking analysis –*

Cultured HUVECs exhibit numerous filopodia, which are actin-rich tubular extensions, >2  $\mu\text{m}$  long and  $\sim 150$  nm in diameter. Some of the filopodia protruded close to the coverslip and were visualized in our video-records by the evanescent field excitation. This provided an opportunity to track GFP-tagged molecules that were essentially constrained to a single dimension independent of the depth,  $z$ , of the evanescent field. The molecule movements were suitable for kymograph analysis. Spline-fits to the overall filopodial shape allow image data to be “straightened” and a linear strip of image pixels was then extracted to form the abscissa in the kymograph time-series image (**Fig S3 in the Supporting Material**).

The  $\beta$  complexes produce punctate images on each video frame and their motion within the filopodium then created a pattern of vertical trajectories (i.e. along the ordinate, time axis). Trajectories consisted of linear, bright segments that were tilted slightly towards the cell body (at  $\sim 1.5$   $\mu\text{m}/\text{min}$ ), consistent with complexes binding tightly to actin and reporting the slow rearward flow of the central F-actin bundle of the filopodium (51). These events were interspersed with haphazard, dim trajectories as the particles dissociated from actin and diffused within the body of the filopodium. Both types of trajectories were observed for closely adjacent objects within the same filopodium over the same time window, indicating that dim trajectories result from mobility of the  $\beta$  complexes within the filopodium rather than movement of the filopodium relative to the glass coverslip.

The time-resolved characterization of bound and free episodes of  $\beta$  molecules constrained within the evanescent field by the filopodia was our initial motivation. However, to our surprise, the kymographs also revealed that  $\alpha$ , as well as  $\beta$  associates with filopodial F-actin.

*6. F-actin dependence of CaMKII  $\alpha$  and  $\beta$  lifetime distributions by evanescent field fluorescence photo-activation microscopy –*

To follow up the finding that both  $\alpha$  and  $\beta$  isoforms bind actin within filopodia we examined the kinetics of fluorescence decay following photo-activation of PaGFP fusion constructs within the cell cortex. A brief flash of TIR laser light, at 405nm, was used to activate PaGFP while continuous illumination at 488nm allowed the activated fluorescence to be visualized. The fluorescence of PaGFP alone decayed rapidly, reaching half its initial value within a single video frame (<50 ms) (**Figure 4A**). The decay was two orders of magnitude more rapid than the photo-bleaching rate estimated from photo-bleaching of immobilized GFP molecules or photo-activation of fixed cells (Materials & Methods). Therefore, the decay must reflect diffusion of the photo-activated PaGFP molecules out of the evanescent field.

The PaGFP-CaMKII fusion constructs (PaGFP- $\alpha$ , PaGFP- $\beta$ ) showed slower and more complex kinetics (**Figure 4A**), though still rapid relative to photo-bleaching. Their fluorescence decay could be followed by single molecule tracking. The decay profiles were approximated by dual-exponential fits with a 0.24s offset relative to the PaGFP intensity decay due to the 5-frame lifetime tracking filter. Direct image field intensity measurements, analogous to those for PaGFP but corrected for the offset, showed a two-fold difference in the fast, but not slow, component decay. Tracks may terminate for reasons other than fluorescence loss that could account for the modest discrepancy; specifically cross-over of tracks of unbound particles and imperfections of the tracking algorithm (Section SA2).

The slow components for PaGFP- $\alpha$  (1.9s) and PaGFP- $\beta$  (3.0s) were incompatible with free diffusion. Therefore, we used latrunculin B (“latrunculin”) (52) to test whether disruption of the actin cytoskeleton affected the mobility of PaGFP-CaMKII fusion proteins. The effect of latrunculin on HUVEC stress fibers was evident within a few minutes (**Figure 4B**). Prior to latrunculin treatment PaGFP- $\alpha$  co-localized weakly generating an anisotropic pattern that aligned with the stress fibre arrays as appreciated by the elliptical Fourier spectra (FT) of the red / green images. Red FT ( $R_{(\text{maj}/\text{min})}$  (major / minor axial ratio)) = 1.35, angle =  $16 \pm 5^\circ$ ); green FT ( $R_{(\text{maj}/\text{min})}$  = 1.33, angle =  $24 \pm 5^\circ$ ). After incubation (10 minutes) with latrunculin the pattern had disappeared (FT  $R_{(\text{maj}/\text{min})} \sim 1$  for both

channels) (**Figure 4B insets**). We measured the photo-activated fluorescence decay kinetics at 0 and 10 minutes after latrunculin treatment. Dual-exponential fits to the fluorescence decrease showed the amplitude and rate of the fast decay component increased with time after treatment, consistent with a reduced, F-actin immobilized fraction (**Figure 4C**). We repeated the experiment with PaGFP- $\beta$ . Photo-activated PaGFP- $\beta$  formed brightly fluorescent filamentous substructures that disappeared following latrunculin treatment. The kinetics of PaGFP- $\beta$  fluorescence decay also changed (**Figure 4D**) concomitant with the observed structural changes. The fluorescence decay following photo-activation revealed a substantial fast-decay component for pulses applied five minutes post-latrunculin treatment. The fast component increased with incubation time so that for photo-activation pulses 15 minutes post-latrunculin the decay was similar to that seen for photo-activated PaGFP- $\alpha$  after 10 minutes post-latrunculin. The fast component decay was consistent with the formation of a GFP-like, inert species.

**Figure 4: PALM TIRFM and latrunculin treatment show both CaMKII isoforms associate with the actin cytoskeleton.** **A.** Normalized fluorescence decay curves of PaGFP and PaGFP-CaMKII fusion proteins following photo-activation by 405nm laser (at  $t=0$ ). Decay was measured as single molecule track lifetimes. Time 0 is time to exceed the 5-frame track duration threshold (0.24s). Data were least-squared fitted to two exponentials (yellow lines): PaGFP- $\alpha = 0.72 \pm 0.01(e^{-15.2 \pm 0.5t}) + 0.28 \pm 0.01(e^{-0.35 \pm 0.07t})$ .  $n=4,306$ ; PaGFP- $\beta = 0.51 \pm 0.01(e^{-3.56 \pm 0.08t}) + 0.49 \pm 0.01(e^{-0.24 \pm 0.07t})$ .  $n=11,160$ . In contrast, photo-activated PaGFP fluorescence intensity measured over the image field decayed over 50% within 0.1s (2 frames). **B.** HUVEC stress-fibers after 10 minute (**10'**) treatment with latrunculin (5  $\mu$ M). Top panels (red) show the averaged tRFP-actin images: although there is little change in the total fluorescence (97 $\pm$ 17 counts/pixel (pre-latrunculin). 100 $\pm$ 23 counts/pixel (post-latrunculin)); the fibers disappear after treatment. Lower panels show PaGFP-CaMKII $\alpha$  (green) and single particle tracks (white lines ( $n = 3,777$  (**0'**), 1,573 (**10'**)) superimposed on actin (red). **Insets:** Fourier spectra (tRFP-actin (red); GFP (green)). **C.** PaGFP-CaMKII $\alpha$  fluorescence decay pre and post-latrunculin treatment: Dual exponential fits; 0.71 $\pm$ 0.01( $e^{-18.1 \pm 0.5t}$ ) + 0.29 $\pm$ 0.01( $e^{-0.39 \pm 0.01t}$ ) (dashed yellow line) (**0'**); 0.8 $\pm$ 0.01( $e^{-19.9 \pm 0.8t}$ ) + 0.21 $\pm$ 0.01( $e^{-0.92 \pm 0.04t}$ ) (dotted yellow line) (**10'**). **D.** Fluorescence intensity decay curves of PaGFP- $\beta$  at various times (in minutes) after addition of latrunculin (5  $\mu$ M) to a Cos7 cell culture. Intensity normalized to unity at  $t = 0s$  ( $t_0$ ) and zero at  $t = 3s$  ( $t_3$ ). ( $t_3/t_0 \sim 50\%$ ). Control fit (un-normalized): (0.26 $\pm$ 0.01) + (0.74 $\pm$ 0.01( $e^{-0.28 \pm 0.01t}$ )). Post-latrunculin fits (green lines): 0.58( $e^{-24.3t}$ ) + 0.42( $e^{-1.2t}$ ) (**10'**); 0.81( $e^{-29.3t}$ ) + 0.19( $e^{-1.8t}$ ) (**15'**). **Inset:** Filamentous structures visualized when PaGFP- $\beta$  was photo-activated in absence of latrunculin (**0'**) were not observed (**10'**) after addition of latrunculin. Correlation coefficient  $R^2 > 0.99$  for all fits.

## B. Structural Determinants of the CaMKII F-actin interaction

Having established single molecule imaging techniques using native  $\alpha$  and  $\beta$  isoforms, we next examined GFP-fusions of a panel of functionally significant CaMKII mutants. The mutations are mapped onto the CaMKII structure in **Figure 5A** (residue positions are incremented by one in the corresponding  $\beta$  sequence). The primary phosphorylation site,  $\alpha$ T286, is important for long-term depression (LTD) as well as LTP since these functions are impaired in  $\langle \alpha$ T286A  $\rangle$  mutant mice (53, 54), and affected or abolished respectively by over-expression of a constitutively active  $\langle \alpha$ T286D  $\rangle$  (55). To explore its role in single-molecule binding to cytoskeletal actin we studied the homologous  $\beta$ T287A and  $\beta$ T287D mutants (1). Phosphorylation of secondary sites,  $\alpha$ T305 and  $\alpha$ T306, is known to inhibit kinase activity (33). We compared differences among  $\alpha$ T286D/T305/T306 triple mutants with both secondary sites mutated to either aspartate or alanine. Other mutations / lesions of interest were  $\alpha$ K42R that blocks ATP binding necessary for CaMKII activation, LTP and spine enlargement

(56);  $\alpha$ A302R that disrupts calmodulin binding and translocation to the PSD (9) and the  $\beta$ E' splice-variant that lacks linker sequences encoded by exons I and IV (57). Finally, we used the tatCN21 inhibitor that competes with the NR2B NMDA receptor subunit for binding to the T-site (58) to see whether CaMKII binding targets elicit structural changes (59) that affect F-actin association.

1. The primary phosphorylation site mutants have dramatically different effects on F-actin binding -

Averaged images show that the phosphorylation incompetent  $\beta$ T287A mutant decorates cortical actin structures (**Figure 5Bi / Fig S4 in the Supporting Material**). In contrast, the  $\beta$ T287D videos (**Movies S2, S3 in the Supporting Material**) showed an isotropic distribution of fast moving spots in the cell cortex that did not map onto the stress fibers (**Figure 5Bii, Fig. S4**). As for  $\beta$ , tracks of immobilized  $\beta$ T287A spots had initial intensities that were several multiples of individual GFP fluorophores and showed multistep photo-bleaching time courses. A rare example of a long-lived track revealed 10 steps (**Figure 5C**), consistent with the intensity ratio of the immobilized  $\beta$ T287A spot relative to single GFP fluorophores. In contrast, averaged images of the phospho-mimetic  $\beta$ T287D mutant showed no evidence of actin co-localization.

The difference between the two mutant proteins was emphasized by analysis of MSD vs.  $\Delta t$  plots (**Figure 5D**). For  $\beta$ T287A, the initial slope and subsequent behavior was superimposable with results obtained using native CaMKII $\beta$ . The addition of tatCN21 (1  $\mu$ M) had no effect on the association of  $\beta$ T287A with F-actin (2 different cultures, > 10,000 tracks). In contrast, the initial (MSD vs.  $\Delta t$ ) slope for  $\beta$ T287D was much greater than for  $\beta$  and  $\beta$ T287A with virtually no (<7%) tracks of duration longer than 0.4s (+0.24s offset) - consistent with fast-moving objects that diffused rapidly out of the evanescent field.

**Figure 5: The T287D point-mutation down-regulates association with the actin cytoskeleton. A.** Atomic structure (3SOA.PDB) of rat CaMKII (18). The positions of the mutated sites (K42 (yellow), T286 (red), A302 (peach), T305 / T306 (magenta)) studied, the junction of kinase (green) and association (blue) domains where the splice E' linker segment would be located, and the substrate binding T-site (white) are shown in relation to the secondary structure elements (cartoon representation). **B.** Superimposed averaged images, processed as in Figure 3A, show localization of single molecules (Fig. S4, Movies S2, S3) of (i) the dephosphorylated mimic,  $\beta$ 287A (550 frames,  $P_{pix} = 0.29$ ,  $P_{rand} = 0.16 \pm 0.07$ ,  $n = 6,511$ ) and (ii) the phospho-mimic,  $\beta$ 287D (475 frames ( $P_{pix} = 0.08$ ,  $P_{rand} = 0.0 \pm 0.08$ ,  $n = 1,020$ )) with tRFP-actin (red, 100 frames). Mean tRFP intensities were  $105 \pm 6$  ( $\beta$ T287A) and  $213 \pm 75$  ( $\beta$ T287D) counts / pixel. **C.** Photo-bleaching profile of a long-lived  $\beta$ 287A-GFP track (upper black line plot) with the corresponding t-test statistic (t-stat) based on a rolling, non-overlapping 12-frame window (lower red line plot). The t-stat axis denotes the probability that successive 12-frame segments have the same mean. The probability threshold was set to  $10^{-5}$  for detection of a step change. The bars on the time axis of the upper plot mark the ten steps identified by the t-test. The mean lifetime and intensity decrease per step was  $2.6 \pm 0.4$  seconds and 15.5 counts/pixel respectively. **D.** Average track MSD vs.  $\Delta t$  plots for the  $\beta$ 287D and  $\beta$ 287A populations. The dashed line is the plot for the native  $\beta$  population redrawn from Figure 3C.

2. All of the mutant isoforms showed similar single object intensities, but formed two distinct mobility groups -

Analysis of variance (ANOVA) was used to test for significant differences in  $D_{lat}$  values for the panel of CaMKII mutants (**Figure 6A**) based on estimates of variance within and between data sets (**Table S1 in the Supporting Material**). Variances were normalized for different degrees of freedom and the probabilities,  $p$ , that differences between populations are significant ( $p < 0.05$ ) were computed. Consistent with visual inspection of the data (**Figure 6A**) results showed two distinct

groups; a low mobility group comprised of the  $\beta$  proteins (native  $\beta$ ,  $\beta$ K43R,  $\beta$ A303R and  $\beta$ T287A) and a high mobility group comprised of all the  $\alpha$  isoform mutants together with  $\beta$ T287D and  $\beta$ E'. A similar pattern was obtained when instantaneous velocities were compared (**Figure S5 in Supporting Material**). The modal, single spot, intensity values (**Figure 6B**) seen across all proteins are similar and vary between 50-80 counts / pixel, 4-6 fold lower than the anticipated value for the CaMKII holoenzyme and 2-fold greater than for single GFP fluorophores. The similar values rule out oligomer aggregation as a possible cause of the mobility differences between species. Brighter spots seen decorating stress fibers in some video-frames are due to PSF overlap of closely opposed spots; but their tracks can be separated provided the spots are not stationary (27). Spot intensity measurements suggest that expression level affects only holoenzyme number not subunit stoichiometry (**Figure S5B**). Disassembly is also not the cause of inter-species mobility differences since the distributions lack peaks for the single GFP intensity and monomeric  $\alpha$  could not be tracked (Results section A2). The intensity histograms of  $\beta$ ,  $\beta$ T287D and  $\alpha$  (**Figure S5C**) are differentiated by their skewness rather than their modes. The skewness reflects long-lived track lifetimes and results from oligomer immobilization on actin stress fibers (as shown in Figure 3A, 5B).

**Figure 6: Characterization of the mutant proteins. A.** Mobility ( $D_{lat}$  (mean  $\pm$  se)) values for the protein populations. Red bars indicate  $\alpha$  isoforms; white bars  $\beta$ -isoforms.  $\beta$ T287D and  $\beta$ E' have mobility similar to the  $\alpha$  proteins. **B.** Mode ( $\pm$  se) intensities for the native and mutant GFP-CaMKII fusion protein populations. Bar color indicates isoform as in A.

### 3. CaMKII dissociation from cytoskeletal actin –

Thus far, our analysis indicates that the track lifetimes for both  $\beta$  and  $\alpha$  are bi-phasic with MSD vs.  $\Delta t$  plots of the short-lived population consistent with diffusion out of the evanescent field (e.g. Figures 3B and 5D). The photo-activation experiments in the presence and absence of latrunculin demonstrate that population track lifetime is dramatically reduced coincident with stress fiber disassembly. The reduction is mainly due to loss of the long-lived population implying these population lifetimes are limited by dissociation from the actin cytoskeleton (Figure 4). With this in mind we used track lifetime histograms to estimate the bound fraction and the F-actin dissociation rate for different CaMKII mutants.

The phospho-mimic,  $\beta$ T287D lifetime was taken as representative of unbound molecules, based on the failure of  $\beta$ T287D to decorate cytoskeletal structures (Figure 5B, Movie S3) and its high mobility (**Figure 6A**). Consistent with this idea the  $\beta$ T287D track lifetime data was also fairly monotonic with single exponential decay; rate constant =  $6.85 \text{ s}^{-1}$  (1 to 0.05,  $R^2 = 0.99$ ) (**Figure S6 in the Supporting Material**). We then fitted all of the other track distributions over this range to a function that assumed there was a non-binding fraction (i.e. like  $\beta$ T287D) and another longer-lived fraction ( $A_0$ ) that represented actin-binding complexes with an unknown, but slower, dissociation rate ( $k$ ) (Equation 3).

$$A_t = A_0(e^{-kt}) + (1 - A_0)(e^{-6.85t}) \quad \text{Equation 3}$$

Cytoskeletal actin content was assumed to be the same for all experiments, consistent with the modest variation ( $127 \pm 49$  counts/pixel) in the mean tRFP-actin intensities in the images (Figures 3, 4, 5). The additional information obtained from Equation 3 is the estimate of the bound ( $A_0$ ) to freely diffusing pools ( $1 - A_0$ ) of molecules and of the dissociation rate,  $k$ , of molecules from the actin cytoskeleton. The bound fraction,  $A_0$ , was  $0.22 \pm 0.02$  for all strong-binding  $\beta$  fusion proteins (minus  $\beta$ E').  $A_0$  was approximately two-fold lower for ( $\alpha$ ) proteins. The overall group pattern was similar to the pattern observed using the  $D_{lat}$  analysis. The  $k$  values were  $2.9 \text{ s}^{-1}$  and  $1.3 \text{ s}^{-1}$  respectively for native ( $\alpha$ ) and ( $\beta$ ), (Figure S6).

Equation 3 will be valid over the complete (1 to 0) range only for homogenous populations that follow single parameter Poisson probability time distributions. This is not the case for the two populations. For the unbound population, as represented by the  $\beta$ T287D proteins, the  $D_{lat}$  value for the most mobile among them ( $\sim 0.5 \mu\text{m}^2/\text{s}$  (Figure 6A)) was  $\sim 18$ -fold lower than the  $D_{Stokes}$  value calculated for free-diffusing ( $\beta$ ) holoenzymes ( $\sim 10 \mu\text{m}^2/\text{s}$ , Equation 1). This discrepancy, as well as the deviation of the  $\beta$ T287D distribution from the single exponential fit (Figure S4), indicates hindered diffusion; though bias introduced by exclusion of rapidly diffusing objects by the 5-frame (0.24 s) track filter will also contribute. Power-law distributions due to hindered diffusion have been characterized for F-actin gels in vitro (60) as well as in vivo for membrane proteins confined by the actin cortex (61, 62). The tRFP-actin labeling does not resolve F-actin single filaments in the dense cortex or F-actin spacing in stress fibers, but limits on physical entrapment may be estimated (**Section B2 in the Supporting Material**). Furthermore, they rule out this scenario for stress fiber decoration. For the bound population, a single  $k$  will obtain only if the dissociation of CaMKII from F-actin subunits does not depend on neighboring subunits. This is not the case since the detachment probability of a subunit is lower if neighboring subunits participate in binding together the CaMKII holoenzymes and F-actin.

Therefore, we re-plotted all our data on log-log axes. We found they deviated markedly from a dual-exponential process once the population fraction was  $< 5\%$  (**Figure 7A**). All distributions showed the same convex log-log relation consistent with a multi-exponential, log-normal distribution of dissociation times. The initial phase of the log plots over which Equation 3 is valid, provides important estimates of the major binding modes. Nevertheless, it was clear that at longer times the data deviated from single parameter, two-population model and this observation was consistent across all data sets.

**Figure 7: Track lifetimes show log-normal decay. A.** Log-log plots of the CaMKII track lifetime distributions deviate from dual exponential fits and show downward curvature, most evident at longer times: (i)  $\beta$  proteins. (ii)  $\alpha$  proteins. **B.** Histogram of rates ( $k_{10}$ ) computed from decay times to 10% amplitude. Asterisks mark species that associate with F-actin.

The times to reach 10% of the initial amplitude ( $t_{1/10}$ ) were compared between data sets (**Figure 7B**) to better represent the log relations. We find the same grouping of different mutants as with the  $D_{lat}$  analysis. ANOVA (**Table S2.I in the Supporting Material**) did not reveal significant differences between the grouped ( $\alpha$ ) proteins; but did so when these were grouped with  $\beta$ T287D,  $\beta E'$ .

As expected,  $t_{1/10}$  for  $\beta$ T287D (1.14+0.02s), the reference unbound state, was lowest; and highest for native  $\beta$  (3.1±0.08s). Differences between the data set were further analyzed by pairwise t-tests against the  $\beta$ T287D reference (**Table S2.II in the Supporting Material**) to parse out differences between group members that were not revealed by the ANOVA. The t-tests revealed  $\alpha$  and  $\alpha$ K2R as outliers within the weak-binding group; while  $t_{1/10}$ 's measured for  $\beta E'$  and the  $\alpha$ T286D proteins with and without secondary phosphorylation site mutations were not significantly different from  $\beta$ T287D (**Figure 7B**).

We used the photo-activation data to estimate the dissociation constants ( $K_D$ )<sup>app</sup> of CaMKII for actin. These provide a more valid estimate of the actin dissociation rate,  $k_{off}$ , since locally activated PaGFP-tagged molecules essentially only leave the evanescent field, whereas GFP-tagged molecules can both exit and enter from the bulk cytoplasm (**Section SB3 in the Supporting Material**), resulting in a 7-fold difference in the observed decay (**Figure 7**). Our  $t_{1/10}$  decay rates for PaGFP- $\alpha$  (3.4±0.4s) and PaGFP- $\beta$  (9.4+0.2s) give  $k_{off}$  ( $=k_{10} ((\log(10))/t_{1/10})$ ) estimates of  $0.68 \text{ s}^{-1}$  and  $0.23 \text{ s}^{-1}$  respectively. If we assume the rate of actin association ( $k_{on}$ ) is at the middle ( $5 \times 10^5 \text{ M}^{-1}\text{s}^{-1}$ ) of the narrow ( $10^5 - 10^6 \text{ M}^{-1}\text{s}^{-1}$ ) diffusion-controlled range (63) applicable to high-ionic strength media such as cell cytoplasm (64), ( $K_D$ )<sup>app</sup> ( $= k_{off}/k_{on}$ ) is 0.5 for  $\beta$  and 1.4  $\mu\text{M}$  for  $\alpha$ . The estimate for  $\beta$  is

### *Single CaMKII molecule binding to F-actin*

comparable to its measured 2.4  $\mu\text{M}$  affinity for G-actin (24). It is consistent with the simplest scenario of a common binding surface for both G and F-actin; though more complex scenarios are possible (65, 66).

## DISCUSSION

We have used TIRFM-based single molecule imaging experiments to study the interaction dynamics of CaMKII isoforms with F-actin within live cultured cells based on dual-color and photo-activation techniques. Our ability to detect micro-molar affinity, weak-binding interactions at sub-second resolution provides complementary information to classical, sedimentation and gel chromatography assays and leads to important new insights.

### 1. The CaMKII binding to cytoskeletal actin –

The mutant analyses characterize CaMKII binding to cytoskeletal actin. **(i)** Substitution of the primary phosphorylated threonine residue by aspartate ( $\beta$ T287D,  $\alpha$ T286D), abolished F-actin association for both isoforms, while substitution with alanine had no effect. The  $\alpha$ T286D mutation abrogated affinity for actin and this effect was independent of mutations at the secondary phosphorylation sites. The  $\beta$ T287A and  $\beta$ T287D, data is consistent with the idea that primary site phosphorylation acts as a single-stage toggle switch, in line with some activation scenarios (67), to control F-actin binding affinity. **(ii)** Consistent with this idea, the  $\beta$ K43R,  $\alpha$ K42R mutations that abolish ATP binding had no effect on F-actin association. Both  $\beta$  and  $\alpha$  isoforms should bind ATP in HUVECs since the CaMKII Michaelis constant for ATP is  $\sim 40 \mu\text{M}$  (59) and cytoplasmic ATP concentration is typically 2-5 mM (68). In addition, the  $\beta$ K43R,  $\alpha$ K42R data show that the CaMKII F-actin association, in contrast to association with receptor subunit GluN2B (69) is insensitive to ATP binding and subsequent hydrolysis *per se*. **(iii)** Elimination of calmodulin binding by the  $\beta$ A303R mutation or use of the peptide inhibitor, tatCN21, had no effect on F-actin association. These observations are most simply consistent with low basal  $\text{Ca}^{2+}$  and CaMKII activity within HUVEC cells. **(iv)** Finally, the splice segment absent in  $\beta\text{E}'$  is essential for actin binding by the  $\beta$  isoform, consistent with sedimentation assays (22).

Using single molecule live cell imaging, we have built upon the initial report of stress fiber decoration in fixed cells (20) that established CaMKII - F-actin interaction. Our direct observation of actin stress fiber decoration by immobilized GFP-CaMKII holoenzymes observed in the presence of a mobile background fraction is consistent with specific binding to F-actin and incompatible with non-specific “entrapment” based on the known stress fiber architecture; as are also the mobility distributions in other actin-rich regions of the cell, based on the known cortical F-actin density and calculated filament mesh size (**Section B2 in Supporting Material**). We found no evidence for higher-order clustering of holoenzymes into larger aggregates that could become either entrapped within, or excluded from, the actin cortical network or stress fibres. The multiple-step photo-bleaching behaviour of static spots and our histogram analysis of single object fluorescence intensities establish that holoenzymes of CaMKII are the predominant species being analysed in our assays. The presence of larger aggregates is further ruled out by the fact that mutations abolishing  $\text{Ca}^{2+}$ /CaM binding (A303R) or nucleotide binding (K42M/K43R) required for aggregate formation (36, 70) did not alter the native  $\alpha / \beta$  mobility and lifetime distributions. Thus, the mobility differences between the  $\beta$ T287D /  $\alpha$ T286D proteins and other CaMKII species, as well as the differences between weak and strong binding groups analyzed in this study can only be explained by differences in F-actin binding affinity.

While CaMKII association with other stress fiber ABPs cannot be eliminated, three considerations argue for direct association with F-actin. First, the ABP would need to be abundantly and uniformly distributed along the fibers to be consistent with our images (Figures 3A / Movie S1; Figure 4A / Movie S2). Other stress fiber structural ABPs,  $\alpha$ -actinin and non-muscle myosin II display periodic banding (43). CaMKII binds to  $\alpha$ -actinin (71) but this binding is not affected by primary site phosphorylation (72) and thus may be ruled out. Second, while activated CaMKII has multiple binding targets, there are few binding partners for inactive CaMKII (2) that, as argued above, may be the dominant form in our HUVEC cultures. Third, relative binding strengths of the CaMKII $\beta$  mutant

proteins in our measurements correlate well with results obtained with synthetic F-actin filaments in bundling assays (22).

In neuronal cultures, differences in dendritic arborization (31) and mobility (32) between native and mutant (A303R, K43R)  $\beta$  GFP fusion proteins have been reported; but these differences are probably due to spontaneous neuronal activity that triggers  $\text{Ca}^{2+}$ .CAM binding for CaMKII activation. Hence, while we do not think multiple binding partners play a role in our assays; they likely do so in dendritic spines. The reported multiple CaMKII kinetic spine subpopulations (16) may also be due, in part, to confinement by, and multimodal interactions with, the F-actin network documented in this study.

### 2. Mechanisms for the log-normal bound life-time distribution –

The estimated dissociation constants,  $(K_D)^{\text{app}}$ , for actin are on the order of  $\mu\text{M}$  for both isoforms. The weak ( $\mu\text{M}$ ) binding of the major  $\beta$  mode is in the ballpark of its reported G-actin affinity. The log-normal distribution of track lifetimes indicates stronger binding modes exist in addition to the dominant initial mode. These modes may arise from engagement of a variable number of CaMKII subunits with one or more actin filaments (**Figure S7**). The fact that the log-normal relation holds for both isoforms and their mutant variants is consistent with the notion that both have a common F-actin binding determinant that is more accessible in  $\beta$  due to its longer more flexible linker. The alternatively spliced linker region encoded by exons I and IV may increase flexibility between subunits comprising the multimeric complex thereby ameliorating geometrical mismatch between CaMKII subunits (73) and binding sites on actin (74). The increased flexibility will optimize contact at the CaMKII and F-actin binding interface, as well as facilitate simultaneous binding at two or more sites thereby increasing binding avidity. The flexibility may also contribute to heterogeneous binding kinetics as single molecule studies indicate that proteins may exist as fluctuating conformational ensembles that lead to power-law distributions in enzyme turnover experiments over the  $10^{-3}$  to 10 second time scale (75). Phosphorylation or substitution of serine / threonine residues within the linker may also attenuate flexibility, based on differences in residue size and charge, to regulate “persistent” CaMKII association with F-actin (13). The possibility that the two isoforms have distinct binding determinants for F-actin cannot be ruled out, but we favor the idea of a common determinant as an explanation based on linker length also accounts for the difference seen between  $\beta$  and  $\beta\text{E}'$

### 3. Physiological implication of the log-normal binding curve –

A log-normal binding curve extends the concentration range for interaction with the actin cytoskeleton. It has two consequences:

First, it explains why the temporal resolution of the assay determines detection sensitivity (**Fig S7 in the Supporting Material**). Ability to discriminate the difference between strong- and weak-binding species will increase as the time-resolution of the assay increases. The likely explanation for the inability of classical assays to detect the weak F-actin binding of  $\langle\alpha\rangle$  is that they only detect long-lived, tight-binding, states. The binding of  $\langle\alpha\rangle$  to F-actin, thus established, must have a physiological rationale. Variations in isoform expression ratios occur as neurons develop. The binding ensures that CaMKII holoenzymes, predominantly composed of  $\alpha$  subunits, can also target the actin cytoskeleton. While the noted functional effects of  $\alpha\text{T286D}$  mutation are thought to be mediated by  $\alpha$  kinase activity, F-actin association may also play a role.  $\langle\alpha\text{T286D}\rangle$  has reduced synaptic localization (76, 77), even though it binds GluN2B *in vitro*; loss of F-actin association could account for this effect.

Second, the curve has implications for the transport of  $\langle\beta\rangle$  down neuronal processes.  $\langle\beta\rangle$  is expressed only in neuronal cell bodies in contrast to  $\langle\alpha\rangle$ . Increased avidity due to binding of multiple subunits to F-actin will depend both on F-actin concentration and geometry as well as CaMKII multimeric state and flexibility. We estimate expression levels of 0.2-0.4  $\mu\text{M}$  in our assays from the density of fluorescent spots in the videos (2000 / 20  $\mu\text{m}^2$  image field area) and 100 nm

## *Single CaMKII molecule binding to F-actin*

effective depth of the evanescent field. CaMKII concentrations in neurons are several-fold higher; above  $\sim 10 \mu\text{M}$  holoenzyme in dendritic spines and  $\sim 2\text{-}5 \mu\text{M}$  holoenzyme in dendritic processes (5). In regions of the cell where the actin cytoskeleton is sparse (i.e. dendritic and axonal branches (78)) the low (micro-molar) affinity of monovalent  $\langle\beta\rangle$  binding would minimize its association with cytoskeletal actin during transport along the long neuronal processes (79). However, in regions where the actin cytoskeleton forms a dense 3D meshwork (i.e. dendritic spines) binding via multiple subunits will be favored and  $\langle\beta\rangle$  will be immobilized. Thus the extended binding range facilitates unhindered transport of CaMKII along neuronal processes and also sequestration at dendritic spines.

Within dendritic spines, the avidity difference between the two isoforms, and between  $\langle\beta\rangle$  and  $\langle\beta\text{E}'\rangle$  will increase; with qualitatively different effects on the spine actin cytoskeleton. High avidity mediated by a few  $\beta$  subunits in the  $\alpha\beta$  hetero-oligomers might be sufficient to stabilize the dynamic actin cytoskeleton. The  $\langle\beta\text{E}'\rangle$  splice variant is expressed in immature neurons (21, 31) when affinity for F-actin, not required for structural remodeling of synaptic sites, would only hinder transport needed for targeted kinase activity. Our results provide a quantitative rationale for why the expression of  $\langle\beta\text{E}'\rangle$  has different physiological effects from  $\langle\beta\rangle$ .

In conclusion, single molecule assays have resolved CaMKII F-actin binding events on the sub-second to second time scale in live mammalian cells. We have documented binding of both neuronal CaMKII isoforms and measured the effect of mutations that act at different points in the CaMKII activation cycle. The behavior of the mutants establishes that binding of CaMKII to actin only occurs when CaMKII is inactive (specifically not phosphorylated at the primary phosphorylation site). This is in contrast to binding of CaMKII to GluNB, which is triggered only when the kinase is active. The new knowledge should be valuable for modeling the role of the actin cytoskeleton in CaMKII transport and synaptic localization.

### *Author Contributions:*

*S.K – Designed and performed research, analyzed data, wrote manuscript.*

*I.C – Performed research.*

*T.C – Contributed reagents.*

*K.U.B – Designed research, contributed reagents, wrote manuscript.*

*J.E.M – Designed research, analyzed data, wrote manuscript.*

*Acknowledgments: We thank Dr Margaret Stratton for comments on the manuscript and Dr Gregory Mashanov for help with computer interfacing and data processing. This work was supported by Royal Society Collaborative Exchange Grant U1175, National Institutes of Health Grant R01-NS081248 (K.U.B), the Molecular Biology Consortium (S.K) and the Francis Crick Institute which receives core funding from Cancer Research UK, UK Medical Research Council, and Wellcome Trust (J.E.M.). The University of Colorado holds the patent rights for tatCN21, its derivatives, and its uses (PCT/US08/077934 “Compositions and methods for improved CaMKII inhibitors and uses thereof”). K.U.B. is owner of Neurexus Therapeutics, LLC.*

*Abbreviations: CaMKII = Calcium calmodulin dependent kinase.  $\langle\alpha\rangle$  = CaMKII $\alpha$ .  $\langle\beta\rangle$  = CaMKII $\beta$ .  $\alpha$  = GFP $\langle\alpha\rangle$ .  $\beta$  = GFP $\langle\beta\rangle$ . PSF = Point spread function. TIRFM = Total internal reflection fluorescence microscopy; ASPT = Automated single particle tracking; HUVEC = human umbilical vein endothelial cells. ABP = Actin binding protein*

## REFERENCES

### SUPPORTING CITATIONS

References (80-86) appear in the Supporting Material

1. Coultrap, S. J., and K. U. Bayer. 2012. CaMKII regulation in information processing and storage. *Trends Neurosci.* 35:607-618.
2. Hell, J. W. 2014. CaMKII: claiming center stage in postsynaptic function and organization. *Neuron* 81:249-265.
3. Hudmon, A., and H. Schulman. 2002. Neuronal CA2+/calmodulin-dependent protein kinase II: the role of structure and autoregulation in cellular function. *Annu. Rev. Biochem.* 71:473-510.
4. Bayer, K. U., J. Lohler, H. Schulman, and K. Harbers. 1999. Developmental expression of the CaM kinase II isoforms: ubiquitous gamma- and delta-CaM kinase II are the early isoforms and most abundant in the developing nervous system. *Brain Res. Mol. Brain Res.* 70:147-154.
5. Otmakhov, N., and J. Lisman. 2012. Measuring CaMKII concentration in dendritic spines. *J. Neurosci. Methods* 203:106-114.
6. Borgesius, N. Z., G. M. van Woerden, G. H. Buitendijk, N. Keijzer, D. Jaarsma, C. C. Hoogenraad, and Y. Elgersma. 2011. betaCaMKII plays a nonenzymatic role in hippocampal synaptic plasticity and learning by targeting alphaCaMKII to synapses. *J. Neurosci.* 31:10141-10148.
7. Dosemeci, A., J. H. Tao-Cheng, L. Vinade, C. A. Winters, L. Pozzo-Miller, and T. S. Reese. 2001. Glutamate-induced transient modification of the postsynaptic density. *Proc. Natl. Acad. Sci. U. S. A.* 98:10428-10432.
8. Shen, K., M. N. Teruel, J. H. Connor, S. Shenolikar, and T. Meyer. 2000. Molecular memory by reversible translocation of calcium/calmodulin-dependent protein kinase II. *Nat. Neurosci.* 3:881-886.
9. Shen, K., and T. Meyer. 1999. Dynamic control of CaMKII translocation and localization in hippocampal neurons by NMDA receptor stimulation. *Science* 284:162-166.
10. Bayer, K. U., and H. Schulman. 2001. Regulation of signal transduction by protein targeting: the case for CaMKII. *Biochem. Biophys. Res. Commun.* 289:917-923.
11. Okamoto, K., T. Nagai, A. Miyawaki, and Y. Hayashi. 2004. Rapid and persistent modulation of actin dynamics regulates postsynaptic reorganization underlying bidirectional plasticity. *Nat. Neurosci.* 7:1104-1112.
12. Hoffman, L., M. M. Farley, and M. N. Waxham. 2013. Calcium-calmodulin-dependent protein kinase II isoforms differentially impact the dynamics and structure of the actin cytoskeleton. *Biochemistry (Mosc).* 52:1198-1207.
13. Kim, K., G. Lakhanpal, H. E. Lu, M. Khan, A. Suzuki, M. K. Hayashi, R. Narayanan, T. T. Luyben, T. Matsuda, T. Nagai, T. A. Blanpied, Y. Hayashi, and K. Okamoto. 2015. A Temporary Gating of Actin Remodeling during Synaptic Plasticity Consists of the Interplay between the Kinase and Structural Functions of CaMKII. *Neuron* 87:813-826.
14. Murakoshi, H., and R. Yasuda. 2012. Postsynaptic signaling during plasticity of dendritic spines. *Trends Neurosci.* 35:135-143.
15. Bayer, K. U., P. De Koninck, A. S. Leonard, J. W. Hell, and H. Schulman. 2001. Interaction with the NMDA receptor locks CaMKII in an active conformation. *Nature* 411:801-805.
16. Lu, H. E., H. D. MacGillavry, N. A. Frost, and T. A. Blanpied. 2014. Multiple spatial and kinetic subpopulations of CaMKII in spines and dendrites as resolved by single-molecule tracking PALM. *J. Neurosci.* 34:7600-7610.

17. Tang, F., and K. Kalil. 2005. Netrin-1 induces axon branching in developing cortical neurons by frequency-dependent calcium signaling pathways. *J. Neurosci.* 25:6702-6715.
18. Chao, L. H., M. M. Stratton, I. H. Lee, O. S. Rosenberg, J. Levitz, D. J. Mandell, T. Kortemme, J. T. Groves, H. Schulman, and J. Kuriyan. 2011. A mechanism for tunable autoinhibition in the structure of a human Ca<sup>2+</sup>/calmodulin-dependent kinase II holoenzyme. *Cell* 146:732-745.
19. Kanaseki, T., Y. Ikeuchi, H. Sugiura, and T. Yamauchi. 1991. Structural features of Ca<sup>2+</sup>/calmodulin-dependent protein kinase II revealed by electron microscopy. *J. Cell Biol.* 115:1049-1060.
20. Shen, K., M. N. Teruel, K. Subramanian, and T. Meyer. 1998. CaMKIIbeta functions as an F-actin targeting module that localizes CaMKIIalpha/beta heterooligomers to dendritic spines. *Neuron* 21:593-606.
21. Lin, Y. C., and L. Redmond. 2008. CaMKIIbeta binding to stable F-actin in vivo regulates F-actin filament stability. *Proc. Natl. Acad. Sci. U. S. A.* 105:15791-15796.
22. O'Leary, H., E. Lasda, and K. U. Bayer. 2006. CaMKIIbeta association with the actin cytoskeleton is regulated by alternative splicing. *Mol. Biol. Cell* 17:4656-4665.
23. Okamoto, K., R. Narayanan, S. H. Lee, K. Murata, and Y. Hayashi. 2007. The role of CaMKII as an F-actin-bundling protein crucial for maintenance of dendritic spine structure. *Proc. Natl. Acad. Sci. U. S. A.* 104:6418-6423.
24. Sanabria, H., M. T. Swulius, S. J. Kolodziej, J. Liu, and M. N. Waxham. 2009. {beta}CaMKII regulates actin assembly and structure. *J. Biol. Chem.* 284:9770-9780.
25. Wong, A. J., T. D. Pollard, and I. M. Herman. 1983. Actin filament stress fibers in vascular endothelial cells in vivo. *Science* 219:867-869.
26. Mashanov, G. I., D. Tacon, A. E. Knight, M. Peckham, and J. E. Molloy. 2003. Visualizing single molecules inside living cells using total internal reflection fluorescence microscopy. *Methods* 29:142-152.
27. Mashanov, G. I., and J. E. Molloy. 2007. Automatic detection of single fluorophores in live cells. *Biophys. J.* 92:2199-2211.
28. Hern, J. A., A. H. Baig, G. I. Mashanov, B. Birdsall, J. E. Corrie, S. Lazareno, J. E. Molloy, and N. J. Birdsall. 2010. Formation and dissociation of M1 muscarinic receptor dimers seen by total internal reflection fluorescence imaging of single molecules. *Proc. Natl. Acad. Sci. U. S. A.* 107:2693-2698.
29. Nenasheva, T. A., G. I. Mashanov, M. Peckham, and J. E. Molloy. 2011. Imaging individual myosin molecules within living cells. *Methods Mol. Biol.* 778:123-142.
30. Nenasheva, T. A., M. Neary, G. I. Mashanov, N. J. Birdsall, R. A. Breckenridge, and J. E. Molloy. 2013. Abundance, distribution, mobility and oligomeric state of M(2) muscarinic acetylcholine receptors in live cardiac muscle. *J. Mol. Cell. Cardiol.* 57:129-136.
31. Fink, C. C., K. U. Bayer, J. W. Myers, J. E. Ferrell, Jr., H. Schulman, and T. Meyer. 2003. Selective regulation of neurite extension and synapse formation by the beta but not the alpha isoform of CaMKII. *Neuron* 39:283-297.
32. Khan, S., T. S. Reese, N. Rajpoot, and A. Shabbir. 2012. Spatiotemporal maps of CaMKII in dendritic spines. *J Comput Neurosci* 33:123-139.
33. Pi, H. J., N. Otmakhov, D. Lemelin, P. De Koninck, and J. Lisman. 2010. Autonomous CaMKII can promote either long-term potentiation or long-term depression, depending on the state of T305/T306 phosphorylation. *J. Neurosci.* 30:8704-8709.
34. Bayer, K. U., E. LeBel, G. L. McDonald, H. O'Leary, H. Schulman, and P. De Koninck. 2006. Transition from reversible to persistent binding of CaMKII to postsynaptic sites and NR2B. *J. Neurosci.* 26:1164-1174.
35. Otmakhov, N., J. H. Tao-Cheng, S. Carpenter, B. Asrican, A. Dosemeci, T. S. Reese, and J. Lisman. 2004. Persistent accumulation of calcium/calmodulin-dependent protein kinase II in dendritic spines after induction of NMDA receptor-dependent chemical long-term potentiation. *J. Neurosci.* 24:9324-9331.

## *Single CaMKII molecule binding to F-actin*

36. Hudmon, A., E. Lebel, H. Roy, A. Sik, H. Schulman, M. N. Waxham, and P. De Koninck. 2005. A mechanism for Ca<sup>2+</sup>/calmodulin-dependent protein kinase II clustering at synaptic and nonsynaptic sites based on self-association. *J. Neurosci.* 25:6971-6983.
37. Khan, S., T. S. Reese, N. Rajpoot, and A. Shabbir. 2012. Spatiotemporal maps of CaMKII in dendritic spines. *J. Comput. Neurosci.* 33:123-139.
38. Subach, F. V., G. H. Patterson, S. Manley, J. M. Gillette, J. Lippincott-Schwartz, and V. V. Verkhusha. 2009. Photoactivatable mCherry for high-resolution two-color fluorescence microscopy. *Nature methods* 6:153-159.
39. Merzlyak, E. M., J. Goedhart, D. Shcherbo, M. E. Bulina, A. S. Shcheglov, A. F. Fradkov, A. Gaintzeva, K. A. Lukyanov, S. Lukyanov, T. W. Gadella, and D. M. Chudakov. 2007. Bright monomeric red fluorescent protein with an extended fluorescence lifetime. *Nature methods* 4:555-557.
40. Goedhart, J., D. von Stetten, M. Noirclerc-Savoye, M. Lelimosin, L. Joosen, M. A. Hink, L. van Weeren, T. W. Gadella, Jr., and A. Royant. 2012. Structure-guided evolution of cyan fluorescent proteins towards a quantum yield of 93%. *Nat Commun* 3:751.
41. Conte, I. L., N. Hellen, R. Bierings, G. I. Mashanov, J. B. Manneville, N. I. Kiskin, M. J. Hannah, J. E. Molloy, and T. Carter. 2016. Interaction between MyRIP and the actin cytoskeleton regulates Weibel-Palade body trafficking and exocytosis. *J. Cell Sci.* 129:592-603.
42. Khan, S., Y. Zou, A. Amjad, A. Gardezi, C. L. Smith, C. Winters, and T. S. Reese. 2011. Sequestration of CaMKII in dendritic spines in silico. *J. Comput. Neurosci.* 31:581-594.
43. Pellegrin, S., and H. Mellor. 2007. Actin stress fibres. *J. Cell Sci.* 120:3491-3499.
44. Burnette, D. T., S. Manley, P. Sengupta, R. Sougrat, M. W. Davidson, B. Kachar, and J. Lippincott-Schwartz. 2011. A role for actin arcs in the leading-edge advance of migrating cells. *Nature cell biology* 13:371-381.
45. Wang, Z., R. Ginnan, I. F. Abdullaev, M. Trebak, P. A. Vincent, and H. A. Singer. 2010. Calcium/Calmodulin-dependent protein kinase II delta 6 (CaMKIIdelta6) and RhoA involvement in thrombin-induced endothelial barrier dysfunction. *J. Biol. Chem.* 285:21303-21312.
46. Dalgaard, P. 2008. *Introductory Statistics with R*. 2nd Edition. Springer, New York. USA.
47. Fischer, H., I. Polikarpov, and A. F. Craievich. 2004. Average protein density is a molecular-weight-dependent function. *Protein Sci.* 13:2825-2828.
48. Swaminathan, R., C. P. Hoang, and A. S. Verkman. 1997. Photobleaching recovery and anisotropy decay of green fluorescent protein GFP-S65T in solution and cells: cytoplasmic viscosity probed by green fluorescent protein translational and rotational diffusion. *Biophys. J.* 72:1900-1907.
49. Swaminathan, R., S. Bicknese, N. Periasamy, and A. S. Verkman. 1996. Cytoplasmic viscosity near the cell plasma membrane: translational diffusion of a small fluorescent solute measured by total internal reflection-fluorescence photobleaching recovery. *Biophys. J.* 71:1140-1151.
50. Rellos, P., A. C. Pike, F. H. Niesen, E. Salah, W. H. Lee, F. von Delft, and S. Knapp. 2010. Structure of the CaMKIIdelta/calmodulin complex reveals the molecular mechanism of CaMKII kinase activation. *PLoS Biol* 8:e1000426.
51. Kerber, M. L., D. T. Jacobs, L. Campagnola, B. D. Dunn, T. Yin, A. D. Sousa, O. A. Quintero, and R. E. Cheney. 2009. A novel form of motility in filopodia revealed by imaging myosin-X at the single-molecule level. *Curr. Biol.* 19:967-973.
52. Coue, M., S. L. Brenner, I. Spector, and E. D. Korn. 1987. Inhibition of actin polymerization by latrunculin A. *FEBS Lett.* 213:316-318.
53. Giese, K. P., N. B. Fedorov, R. K. Filipkowski, and A. J. Silva. 1998. Autophosphorylation at Thr286 of the alpha calcium-calmodulin kinase II in LTP and learning. *Science* 279:870-873.

54. Coultrap, S. J., R. K. Freund, H. O'Leary, J. L. Sanderson, K. W. Roche, M. L. Dell'Acqua, and K. U. Bayer. 2014. Autonomous CaMKII mediates both LTP and LTD using a mechanism for differential substrate site selection. *Cell Rep* 6:431-437.
55. Mayford, M., M. E. Bach, Y. Y. Huang, L. Wang, R. D. Hawkins, and E. R. Kandel. 1996. Control of memory formation through regulated expression of a CaMKII transgene. *Science* 274:1678-1683.
56. Yamagata, Y., S. Kobayashi, T. Umeda, A. Inoue, H. Sakagami, M. Fukaya, M. Watanabe, N. Hatanaka, M. Totsuka, T. Yagi, K. Obata, K. Imoto, Y. Yanagawa, T. Manabe, and S. Okabe. 2009. Kinase-dead knock-in mouse reveals an essential role of kinase activity of Ca<sup>2+</sup>/calmodulin-dependent protein kinase II $\alpha$  in dendritic spine enlargement, long-term potentiation, and learning. *J. Neurosci.* 29:7607-7618.
57. Brocke, L., M. Srinivasan, and H. Schulman. 1995. Developmental and regional expression of multifunctional Ca<sup>2+</sup>/calmodulin-dependent protein kinase isoforms in rat brain. *J. Neurosci.* 15:6797-6808.
58. Vest, R. S., K. D. Davies, H. O'Leary, J. D. Port, and K. U. Bayer. 2007. Dual mechanism of a natural CaMKII inhibitor. *Mol. Biol. Cell* 18:5024-5033.
59. Raveendran, R., S. Devi Suma Priya, M. Mayadevi, M. Steephan, T. R. Santhoshkumar, J. Cheriyan, R. Sanalkumar, K. K. Pradeep, J. James, and R. V. Omkumar. 2009. Phosphorylation status of the NR2B subunit of NMDA receptor regulates its interaction with calcium/calmodulin-dependent protein kinase II. *J. Neurochem.* 110:92-105.
60. Schmidt, C. F., Barmann, M., Isenberg, G., and Sackmann, E. 1989. Chain dynamics, mesh size and diffusive transport in networks of polymerized actin. A quasielastic light scattering and microfluorescence study. *Macromolecules* 22:3638-3649.
61. Heinemann, F., S. K. Vogel, and P. Schwill. 2013. Lateral membrane diffusion modulated by a minimal actin cortex. *Biophys. J.* 104:1465-1475.
62. Umemura, Y. M., M. Vrljic, S. Y. Nishimura, T. K. Fujiwara, K. G. Suzuki, and A. Kusumi. 2008. Both MHC class II and its GPI-anchored form undergo hop diffusion as observed by single-molecule tracking. *Biophys. J.* 95:435-450.
63. Schlosshauer, M., and D. Baker. 2004. Realistic protein-protein association rates from a simple diffusional model neglecting long-range interactions, free energy barriers, and landscape ruggedness. *Protein Sci.* 13:1660-1669.
64. Fersht, A. 1999. *Structure and mechanism in protein science.* W.H Freeman & Co, New York.
65. Dominguez, R. 2004. Actin-binding proteins--a unifying hypothesis. *Trends Biochem. Sci.* 29:572-578.
66. dos Remedios, C. G., D. Chhabra, M. Kekic, I. V. Dedova, M. Tsubakihara, D. A. Berry, and N. J. Nosworthy. 2003. Actin binding proteins: regulation of cytoskeletal microfilaments. *Physiol. Rev.* 83:433-473.
67. Thaler, C., S. V. Koushik, H. L. Puhl, 3rd, P. S. Blank, and S. S. Vogel. 2009. Structural rearrangement of CaMKII $\alpha$  catalytic domains encodes activation. *Proc. Natl. Acad. Sci. U. S. A.* 106:6369-6374.
68. Sachs, J. R. 1981. Internal potassium stimulates the sodium-potassium pump by increasing cell ATP concentration. *J Physiol* 319:515-528.
69. O'Leary, H., W. H. Liu, J. M. Rorabaugh, S. J. Coultrap, and K. U. Bayer. 2011. Nucleotides and phosphorylation bi-directionally modulate Ca<sup>2+</sup>/calmodulin-dependent protein kinase II (CaMKII) binding to the N-methyl-D-aspartate (NMDA) receptor subunit GluN2B. *J. Biol. Chem.* 286:31272-31281.
70. Vest, R. S., H. O'Leary, and K. U. Bayer. 2009. Differential regulation by ATP versus ADP further links CaMKII aggregation to ischemic conditions. *FEBS Lett.* 583:3577-3581.
71. Walikonis, R. S., A. Oguni, E. M. Khorosheva, C. J. Jeng, F. J. Asuncion, and M. B. Kennedy. 2001. Densin-180 forms a ternary complex with the ( $\alpha$ )-subunit of Ca<sup>2+</sup>/calmodulin-dependent protein kinase II and ( $\alpha$ )-actinin. *J. Neurosci.* 21:423-433.

72. Robison, A. J., R. K. Bartlett, M. A. Bass, and R. J. Colbran. 2005. Differential modulation of Ca<sup>2+</sup>/calmodulin-dependent protein kinase II activity by regulated interactions with N-methyl-D-aspartate receptor NR2B subunits and alpha-actinin. *J. Biol. Chem.* 280:39316-39323.
73. Rosenberg, O. S., S. Deindl, L. R. Comolli, A. Hoelz, K. H. Downing, A. C. Nairn, and J. Kuriyan. 2006. Oligomerization states of the association domain and the holoenzyme of Ca<sup>2+</sup>/CaM kinase II. *FEBS J* 273:682-694.
74. Wu, Y., and J. Ma. 2004. Refinement of F-actin model against fiber diffraction data by long-range normal modes. *Biophys. J.* 86:116-124.
75. Min, W., and X. S. Xie. 2006. Kramers model with a power-law friction kernel: dispersed kinetics and dynamic disorder of biochemical reactions. *Phys Rev E Stat Nonlin Soft Matter Phys* 73:010902.
76. Marsden, K. C., A. Shemesh, K. U. Bayer, and R. C. Carroll. 2010. Selective translocation of Ca<sup>2+</sup>/calmodulin protein kinase IIalpha (CaMKIIalpha) to inhibitory synapses. *Proc. Natl. Acad. Sci. U. S. A.* 107:20559-20564.
77. Barcomb, K., I. Buard, S. J. Coultrap, J. R. Kulbe, H. O'Leary, T. A. Benke, and K. U. Bayer. 2014. Autonomous CaMKII requires further stimulation by Ca<sup>2+</sup>/calmodulin for enhancing synaptic strength. *FASEB J.* 28:3810-3819.
78. Xu, K., G. Zhong, and X. Zhuang. 2013. Actin, spectrin, and associated proteins form a periodic cytoskeletal structure in axons. *Science* 339:452-456.
79. Adamec, R., M. Hebert, J. Blundell, and R. F. Mervis. 2012. Dendritic morphology of amygdala and hippocampal neurons in more and less predator stress responsive rats and more and less spontaneously anxious handled controls. *Behav. Brain Res.* 226:133-146.
80. Patterson, G. H. 2007. Photobleaching and photoactivation of fluorescent proteins for studies in cell biology. *Microsc Microanal* 13.
81. Schneider, C. A., W. S. Rasband, and K. W. Eliceiri. 2012. NIH Image to ImageJ: 25 years of image analysis. *Nature methods* 9:671-675.
82. Manders, E. M., Verbeek, F.J and Aten, J.A. 1993. Measurement of co-localization of objects in dual-colour confocal images. *J. Microscopy* 169:375-382.
83. Costes, S. V., D. Daelemans, E. H. Cho, Z. Dobbin, G. Pavlakis, and S. Lockett. 2004. Automatic and quantitative measurement of protein-protein colocalization in live cells. *Biophys. J.* 86:3993-4003.
84. Qian, H., M. P. Sheetz, and E. L. Elson. 1991. Single particle tracking. Analysis of diffusion and flow in two-dimensional systems. *Biophys. J.* 60:910-921.
85. Meyer, R. K., and U. Aebi. 1990. Bundling of actin filaments by alpha-actinin depends on its molecular length. *J. Cell Biol.* 110:2013-2024.
86. Koestler, S. A., K. Rottner, F. Lai, J. Block, M. Vinzenz, and J. V. Small. 2009. F- and G-actin concentrations in lamellipodia of moving cells. *PLoS one* 4:e4810.

# TIRF Workstation

Stage Position

X, Y

Sample

Shutters

Laser 1

Objective lens  
focus

Z

Laser 2

TIR beam

Laser 3

Filters

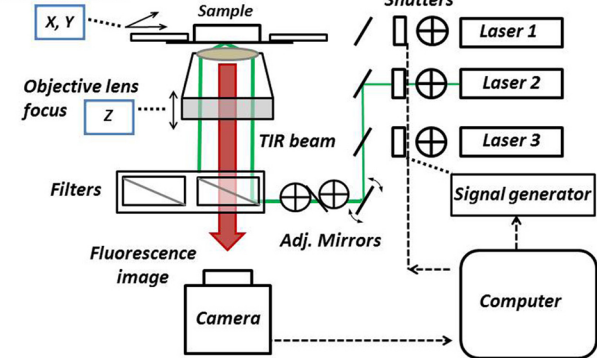
Signal generator

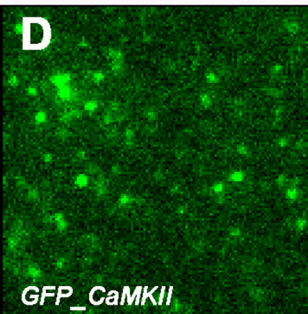
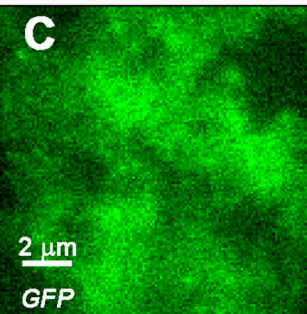
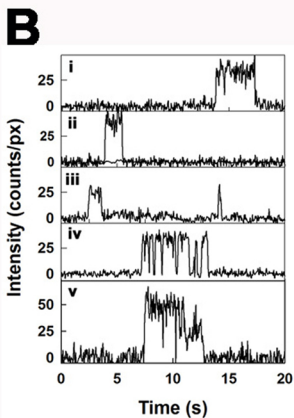
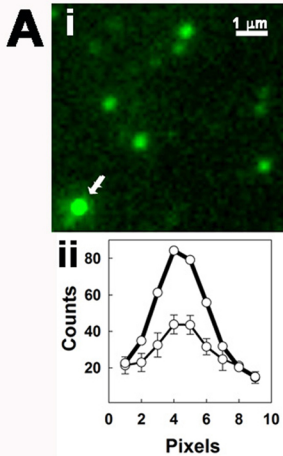
Adj. Mirrors

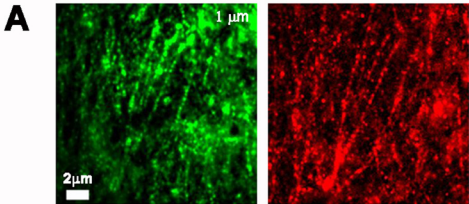
Fluorescence  
image

Camera

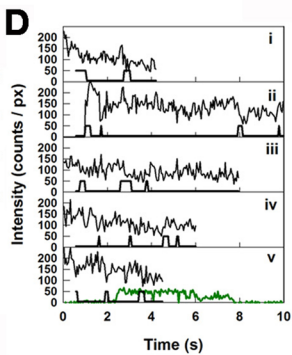
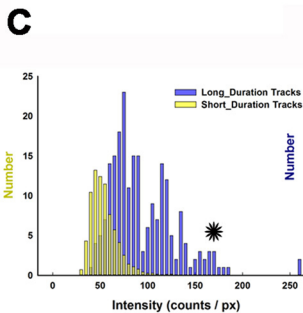
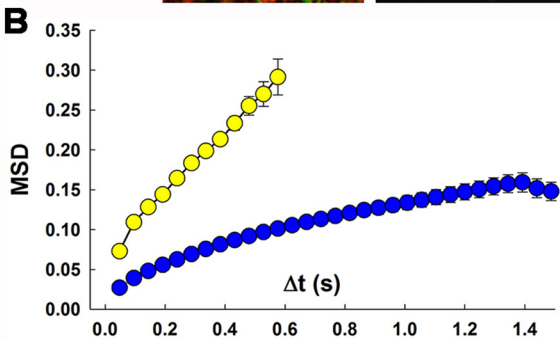
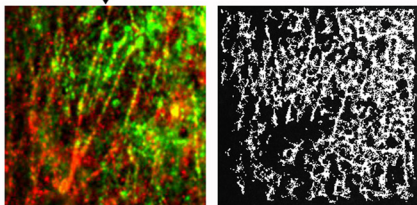
Computer

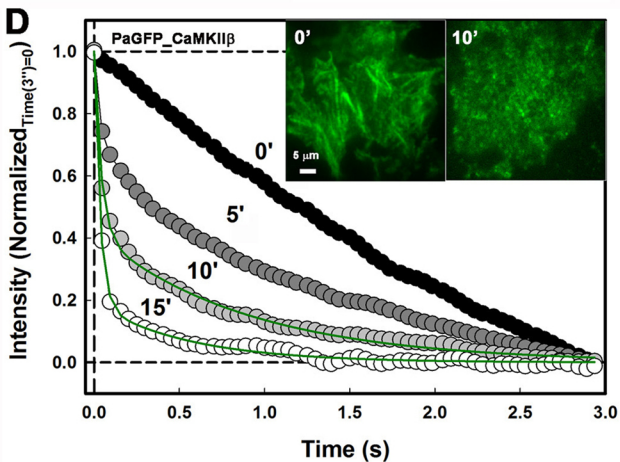
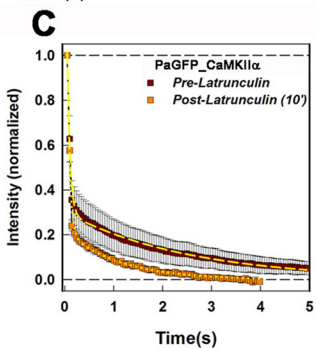
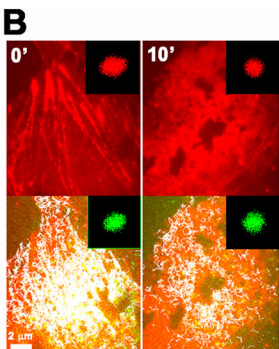
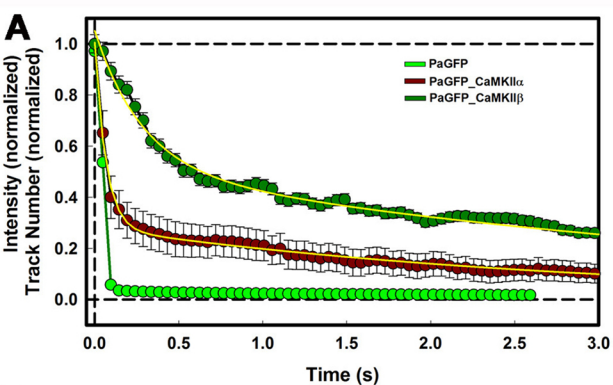


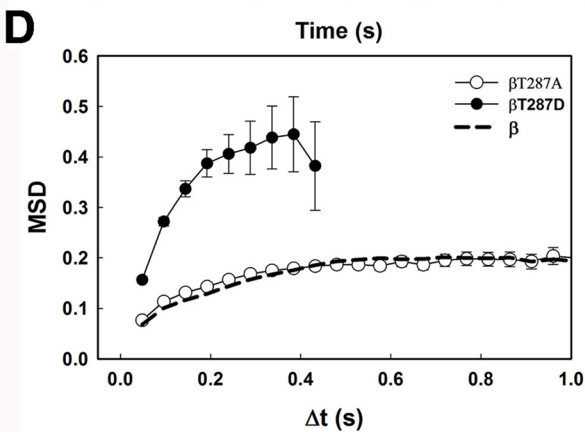
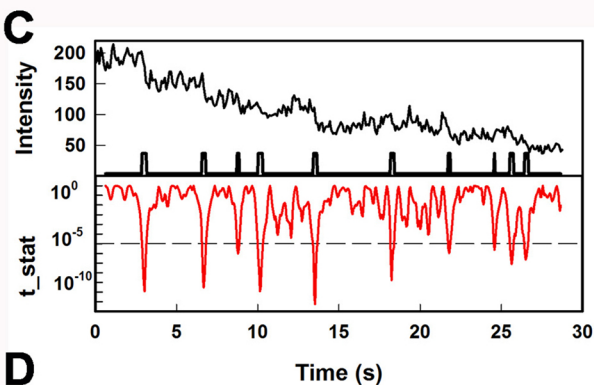
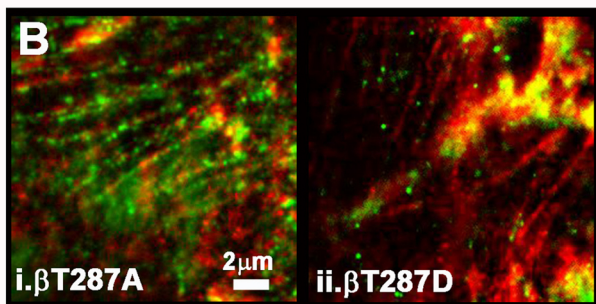
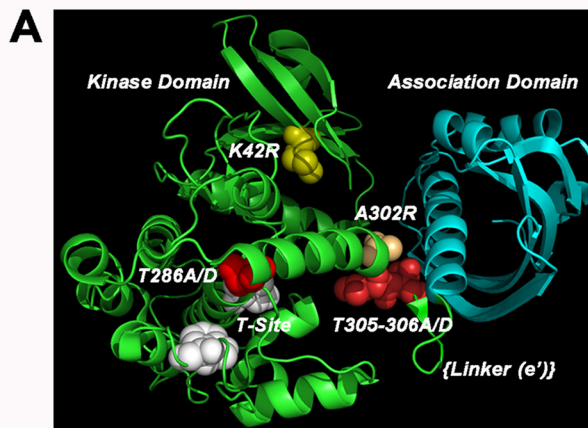


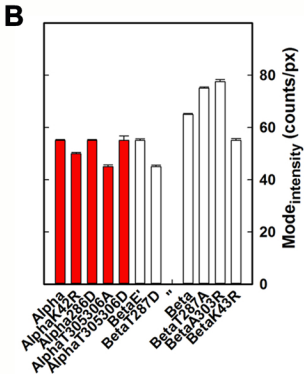
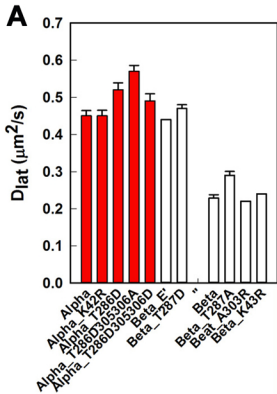


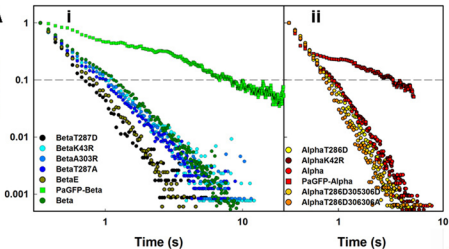
CaMKII $\beta$









**A****B**